

Supporting Information for “Efficient Super-Resolution of Near-Surface Climate Modeling Using the Fourier Neural Operator”

Peishi Jiang¹, Zhao Yang¹, Jiali Wang², Chenfu Huang³, Pengfei Xue^{2,3}, TC

Chakraborty¹, Xingyuan Chen¹, Yun Qian¹

¹Pacific Northwest National Laboratory, Richland, WA, USA

²Argonne National Laboratory, Lemont, IL, USA

³Michigan Technological University, Houghton, MI, USA

Contents of this file

1. Table S1
2. Figures S1 to S17

Introduction The supporting information provides the supplementary table and figures referenced in the main article.

	$\overline{NSE/mKGE}$ – 4km			
	T_2	RH_2	SH	PSFC
FNO-base	0.809/0.886	0.593/0.751	-160.452/0.231	0.939/0.941
FNO-cc	0.819/0.879	0.627/0.757	-172.946/0.477	0.943/0.939
FNO- RH_2	0.809/0.872	0.538/0.739	-161.610/0.161	0.936/0.942
FNO-1kmonly	-0.412/0.530	0.113/0.623	-1542.553/-0.041	0.785/0.843
U-Net	0.881/0.911	0.695/0.790	-20.082/0.637	0.929/0.946
	$\overline{NSE/mKGE}$ – 1km			
	T_2	RH_2	SH	PSFC
FNO-base	0.704/0.884	0.480/0.773	0.576/0.817	0.928/0.939
FNO-cc	0.784/0.899	0.541/0.778	0.666/0.842	0.936/0.943
FNO- RH_2	0.714/0.890	0.454/0.766	0.604/0.826	0.928/0.939
FNO-1kmonly	-0.196/0.563	0.277/0.668	-0.130/0.507	0.786/0.860
U-Net	n/a	n/a	n/a	n/a

Table S1. The performance of the trained deep learning models listed in Table 2 in generating the four near-surface heat states at 4-km and 1-km resolutions on the test period, using the mean of NSE and mKGE.

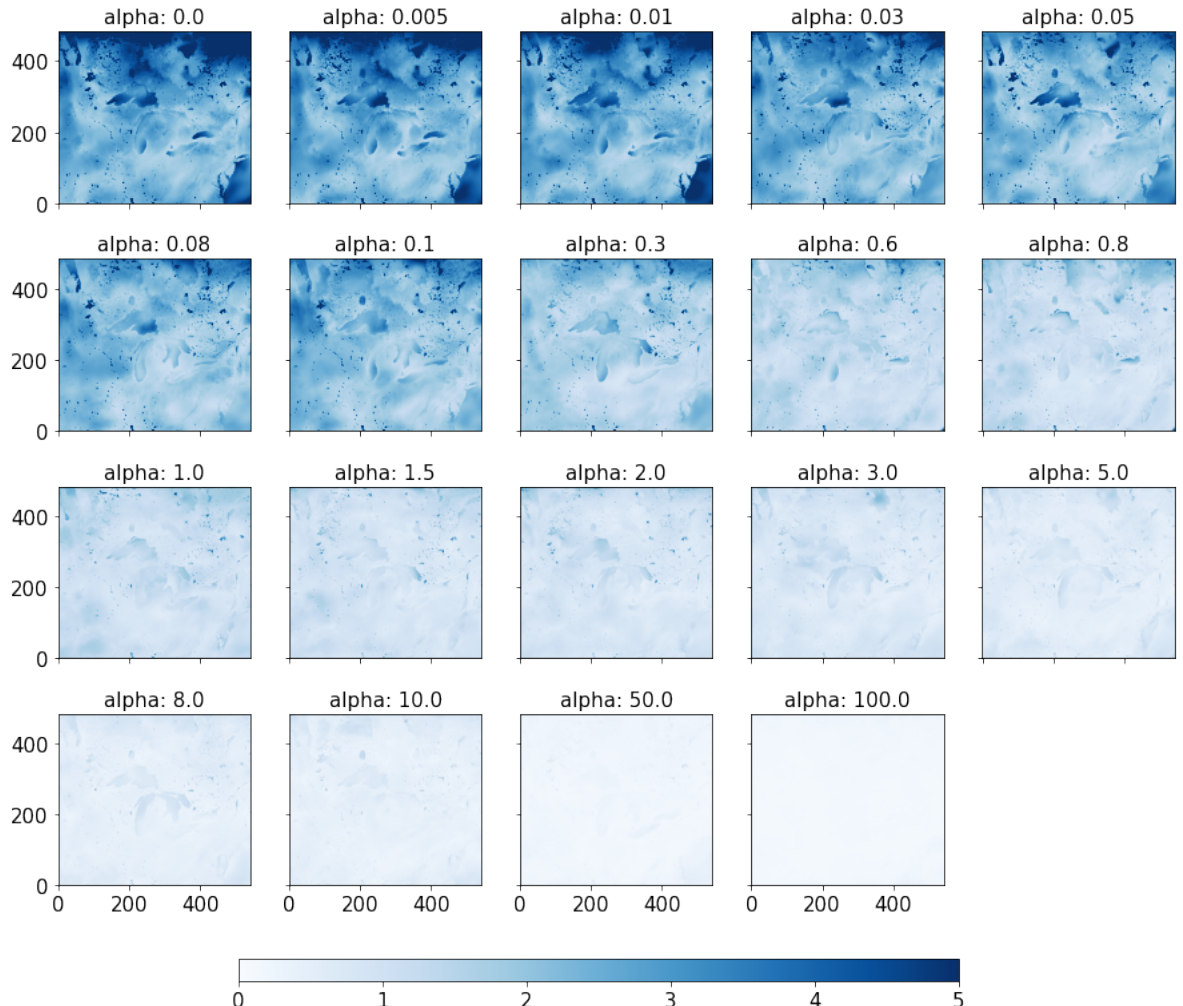


Figure S1. The spatial maps of the temporally averaged absolute difference between the RH_2 emulated by FNO and the corresponding RH_2 computed by Eq.(6) in the main manuscript using varying α . The reduced absolute difference shows the enhanced constraints among the four emulated surface heat dynamics (i.e., T_2 , RH_2 , $PSFC$, and SH) that follows the Clausius–Clapeyron relation in Eq.(6).

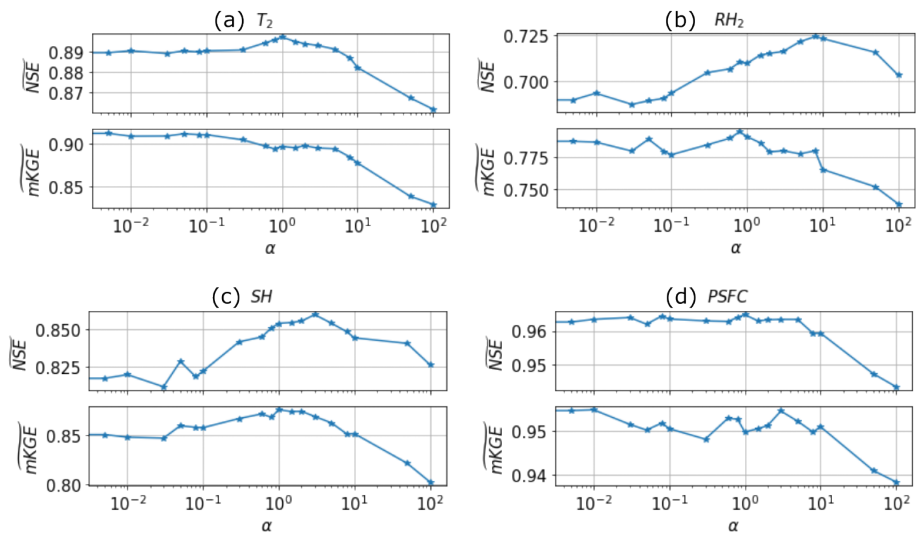


Figure S2. The impact of the physics-constraint loss in Eq.(7): (a)-(d) the computed \overline{NSE} and \overline{mKGE} against different α for the 2-m temperature (T_2), 2-m relative humidity (RH_2), specific humidity (SH), and surface pressure ($PSFC$), respectively, with $\alpha=[0.005, 0.01, 0.03, 0.05, 0.08, 0.1, 0.3, 0.6, 0.8, 1., 1.5, 2., 3., 5., 8., 10., 50., 100.]$.

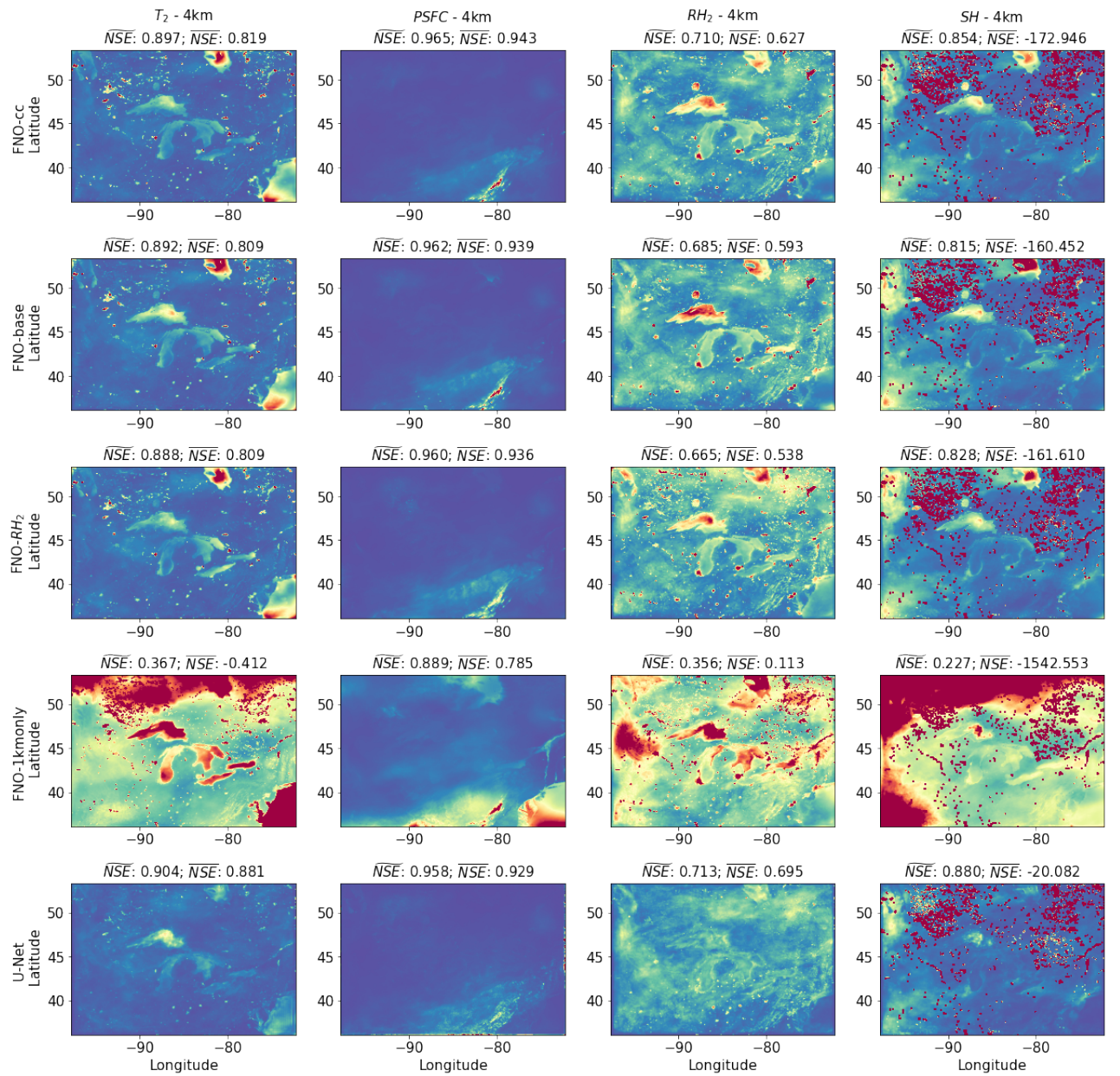


Figure S3. The spatially distributed NSE of all deep learning models at 4-km resolution.

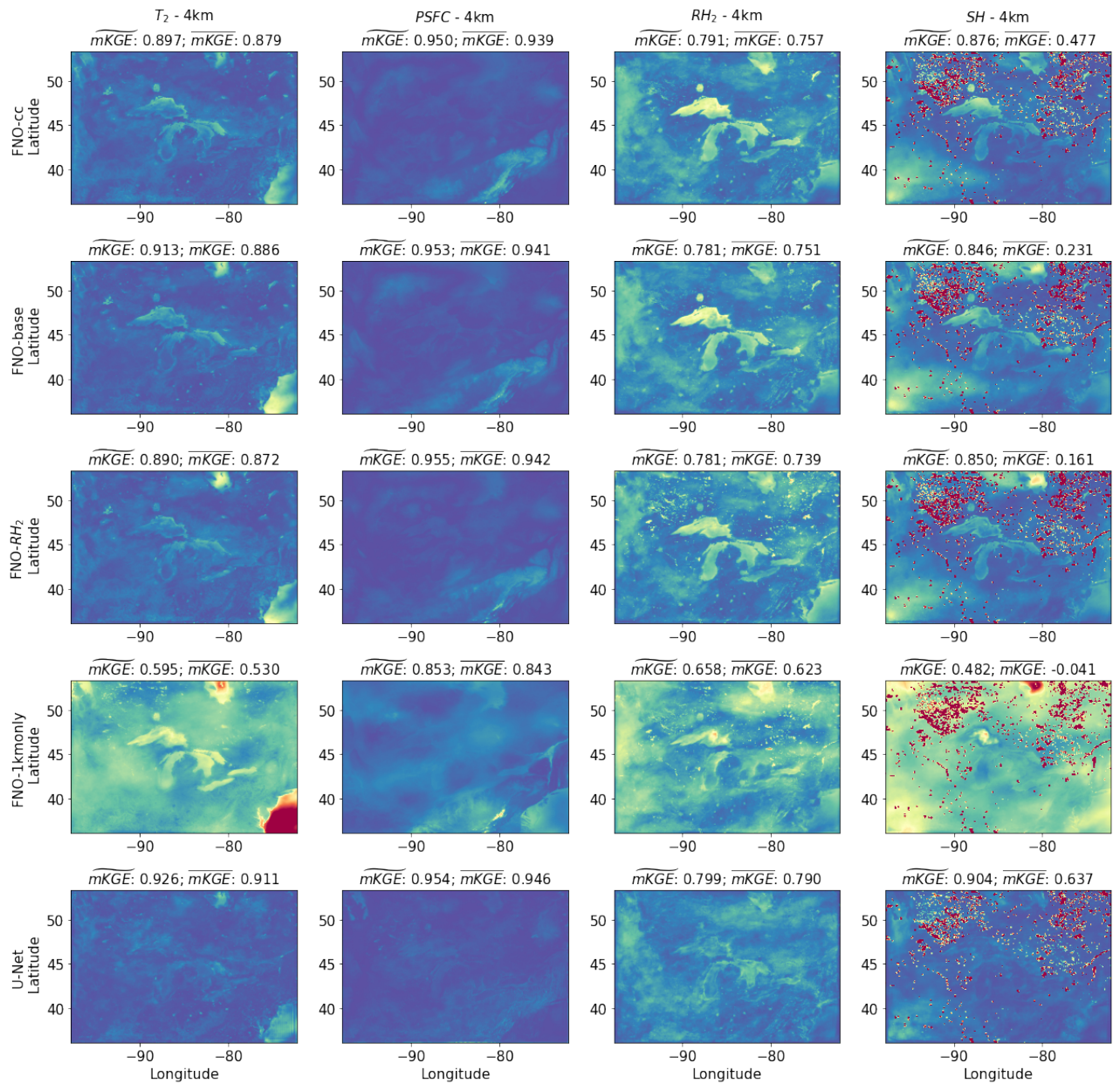


Figure S4. The spatially distributed mKGE of all deep learning models at 4-km resolution.

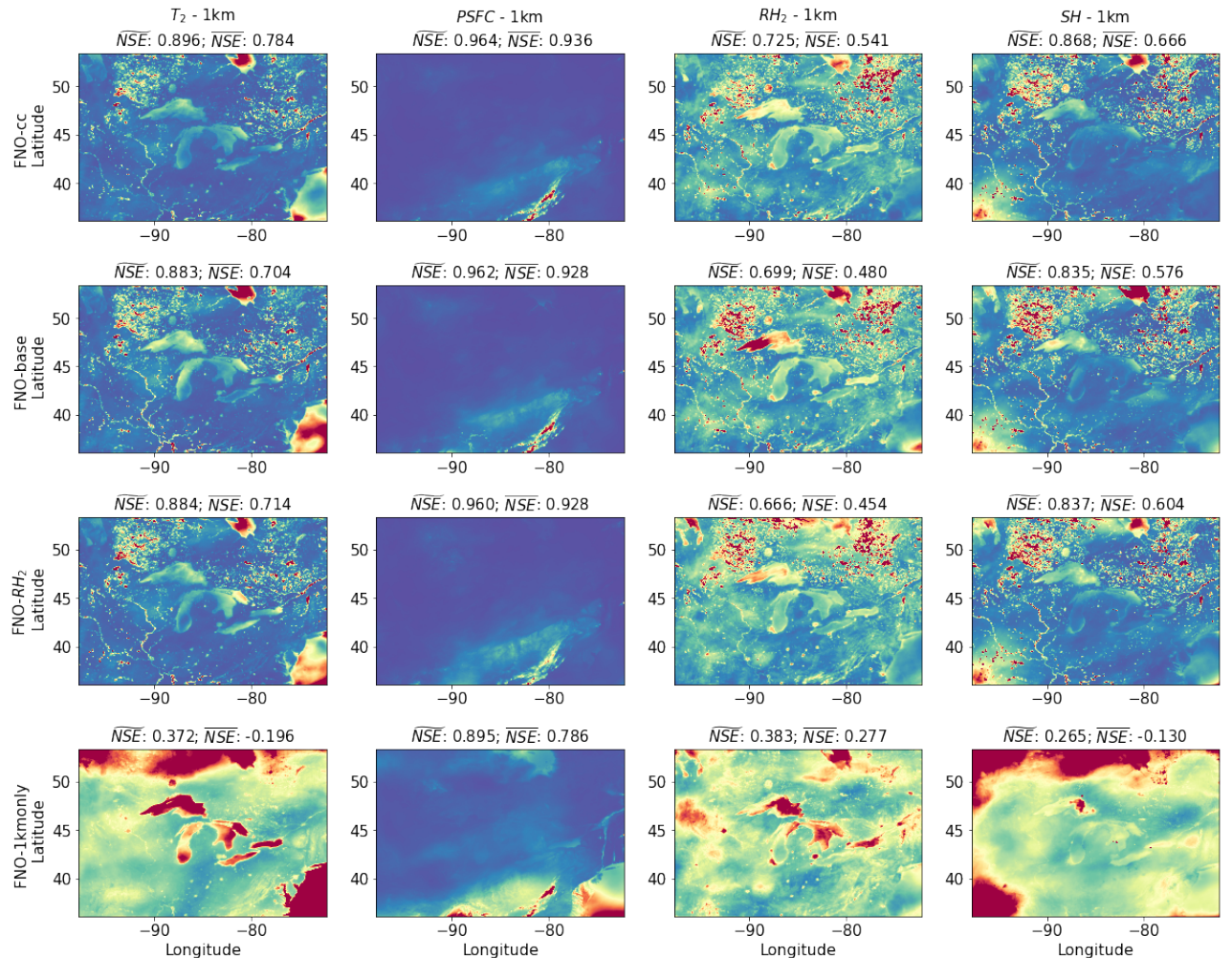


Figure S5. The spatially distributed NSE of all deep learning models at 1-km resolution.

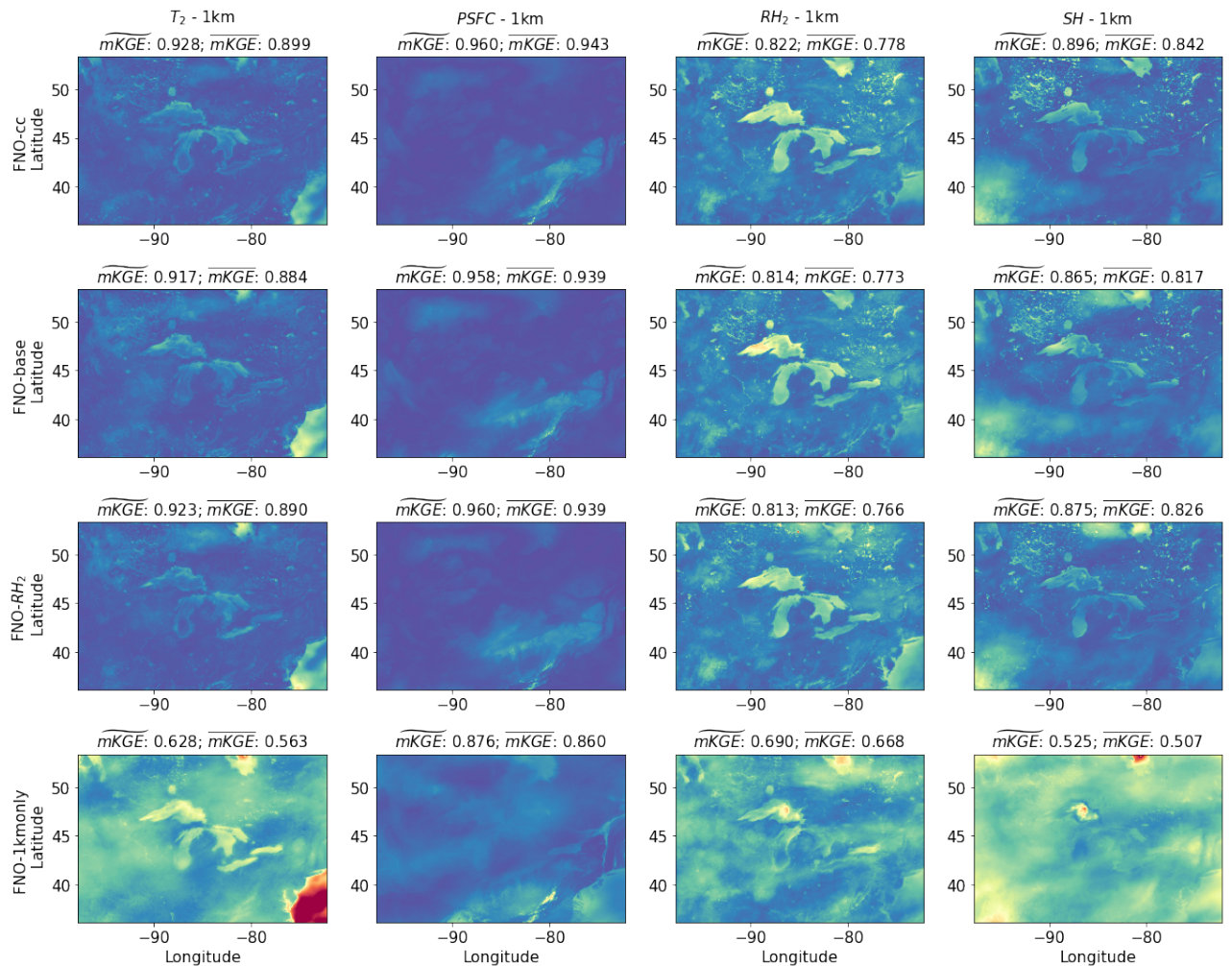


Figure S6. The spatially distributed $mKGE$ of all deep learning models at 1-km resolution.

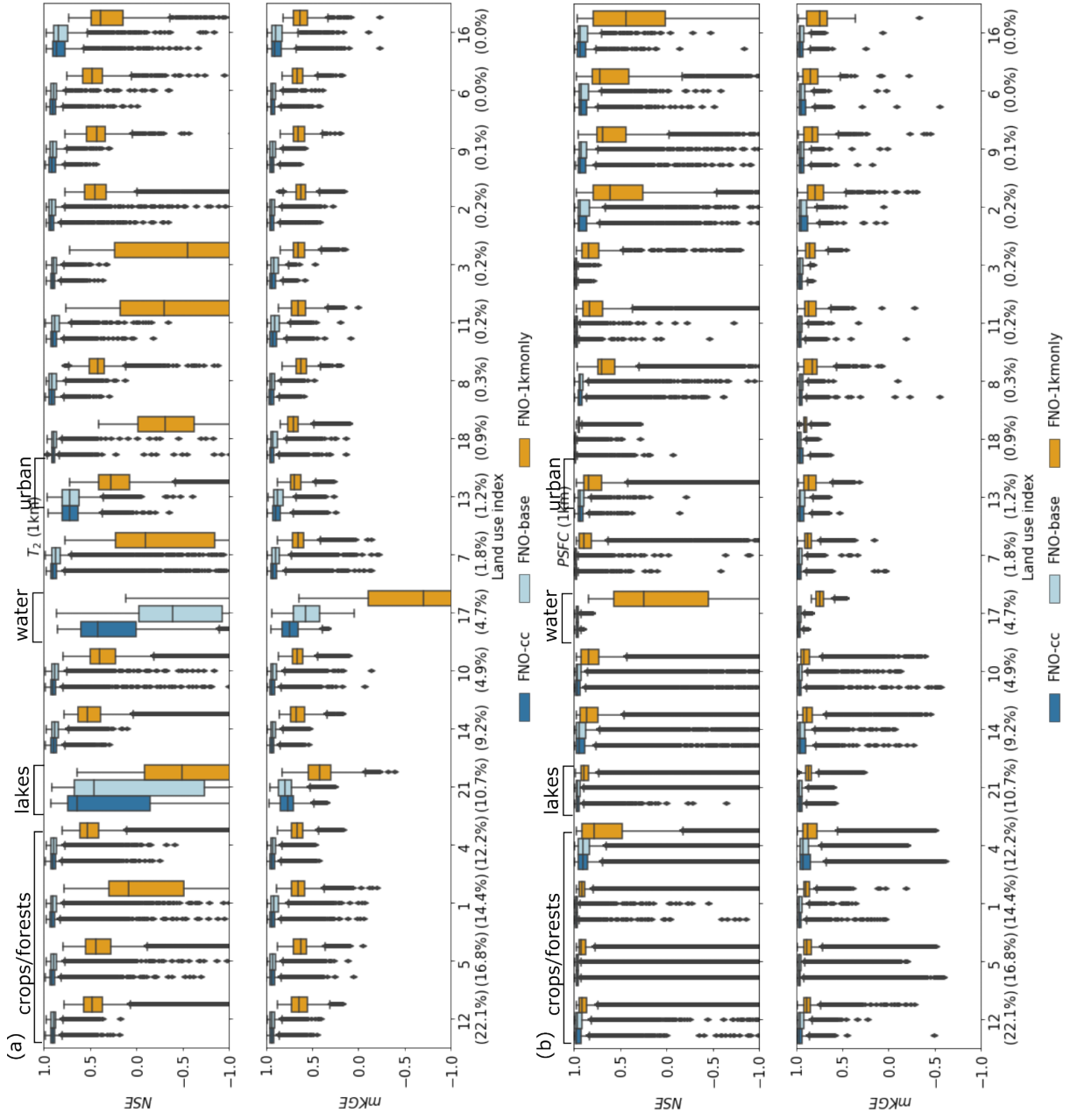


Figure S7. The impact of land use on the 1-km downscaling of FNO-cc, FNO-base, and FNO-1kmonly on the temperature and pressure fields (with $\alpha = 1$): (a) the boxplots of NSE and mKGE values of 2-m temperature (T_2) against each land use index ranked by its proportion in the overall number of spatial grids. (b) the corresponding plots for surface pressure ($PSFC$). (See Table 1 for the detailed description of each land use index.)

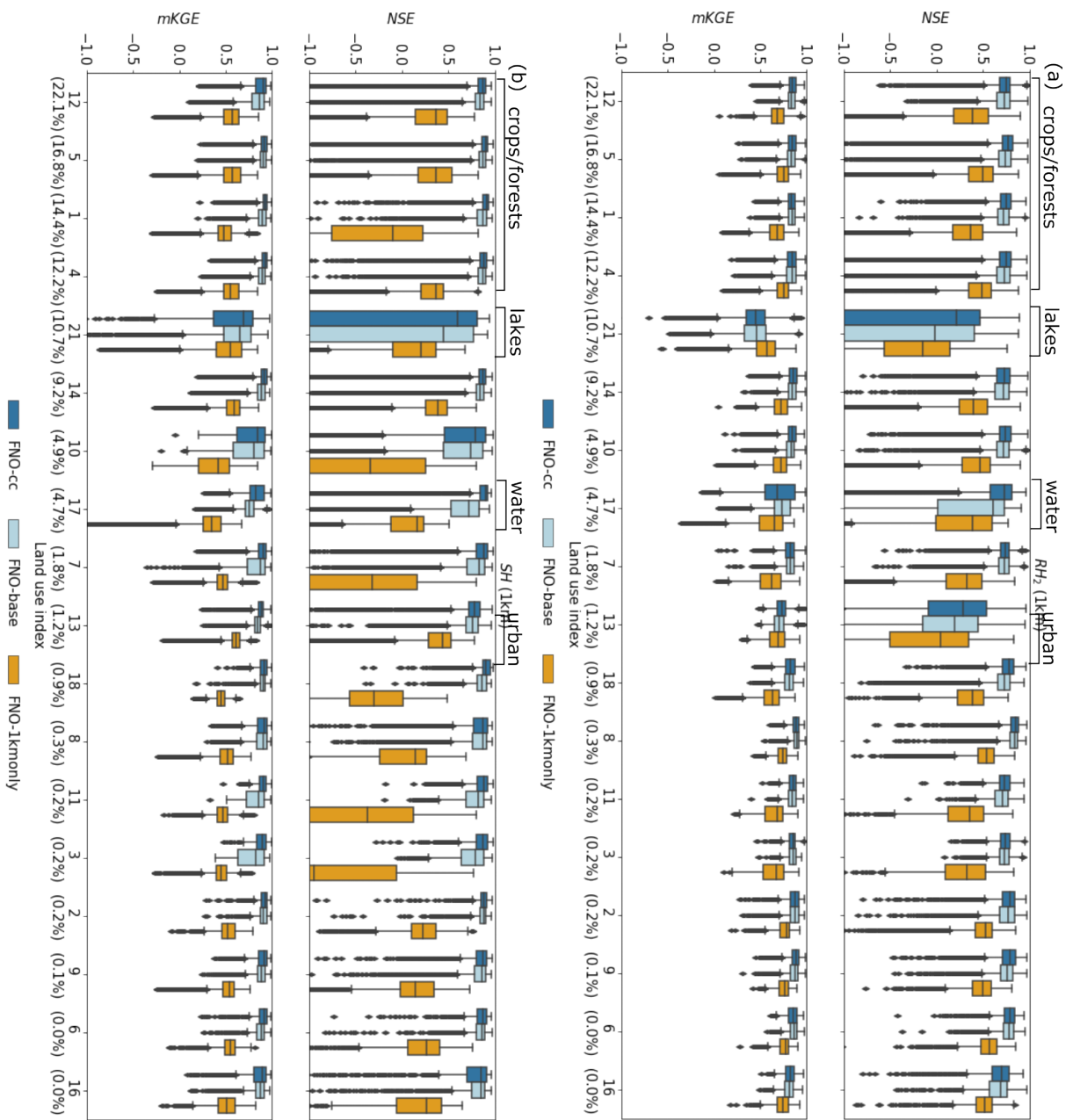


Figure S8. The impact of land use on the 1-km downscaling of FNO-cc, FNO-base, and FNO-1kmonly on the humidity fields (with $\alpha = 1$): (a) the boxplots of NSE and $mKGE$ values of 2-m relative humidity (RH_2) against each land use index ranked by its proportion in the overall number of spatial grids. (b) the corresponding plots for specific humidity (SH). (See Table 1 for the detailed description of each land use index.).

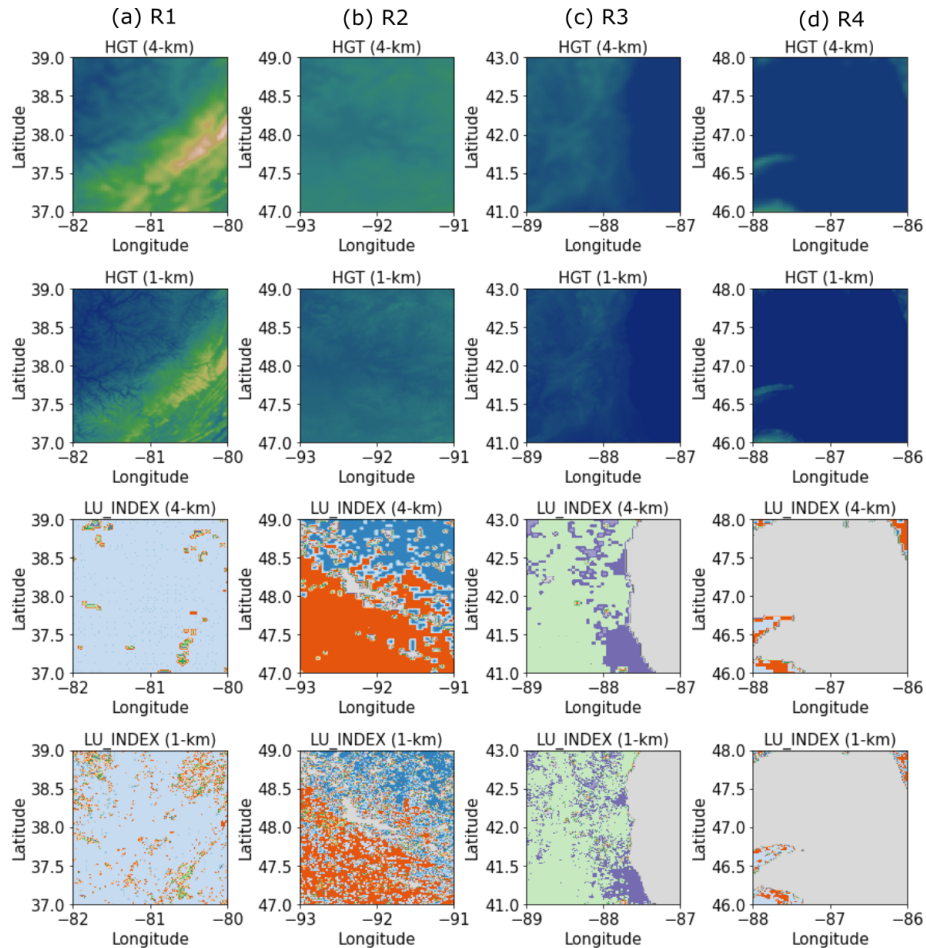


Figure S9. The spatial terrain heights and land use indices of the four subregions (R1-R4) whose geographical locations in the modeling domain are shown in Figure 11 in the main manuscript.

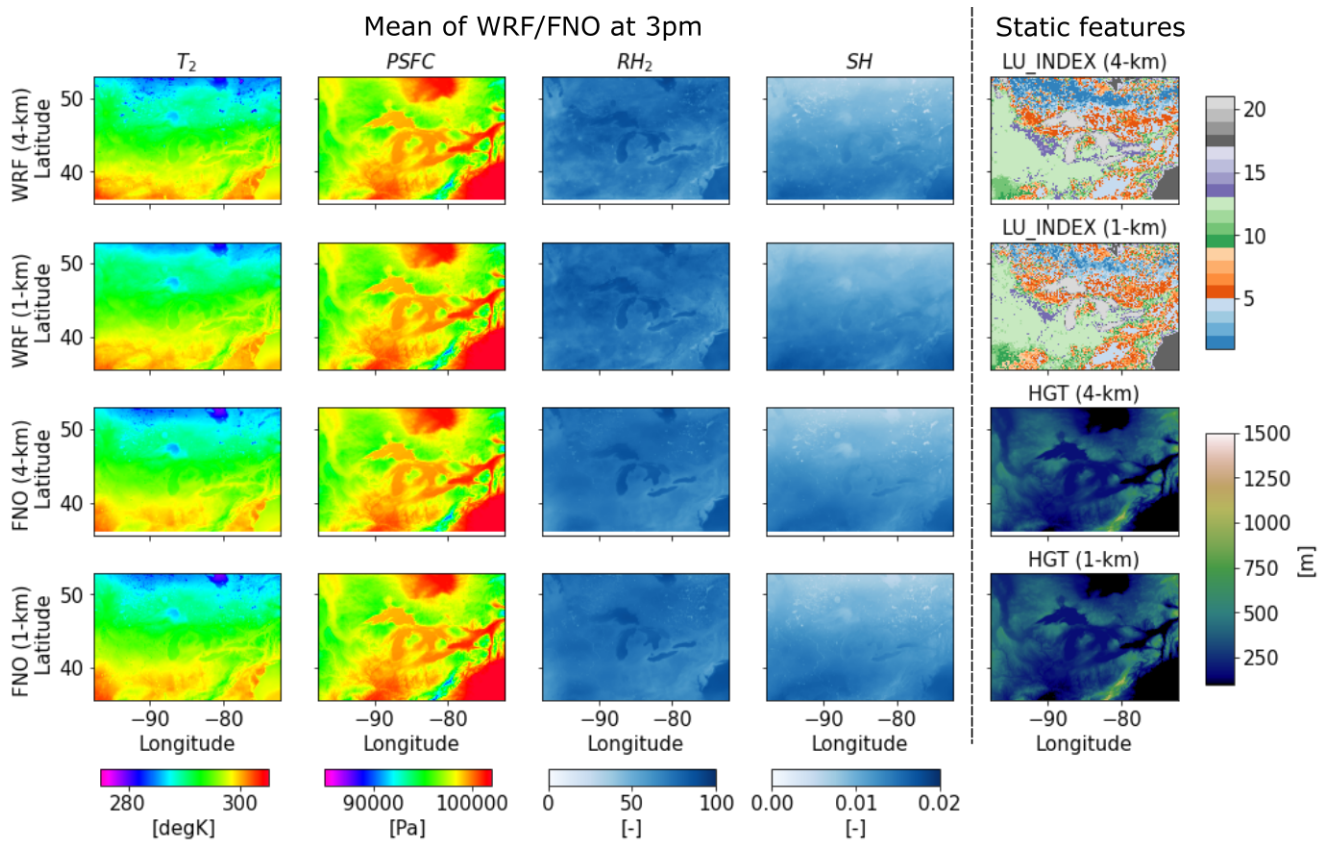


Figure S10. Temporally-averaged WRF and FNO-cc (with $\alpha = 1$) surface heat simulation at 3pm of the entire modeling domain during August-23-2018 through August-31-2018 (i.e., the test period). The right column is the land use index (LU_INDEX) and terrain height (HGT) at both 1-km and 4-km scales. The left four columns are the simulations on the four surface heat variables at R1, including both WRF and FNO simulations at the two scales.

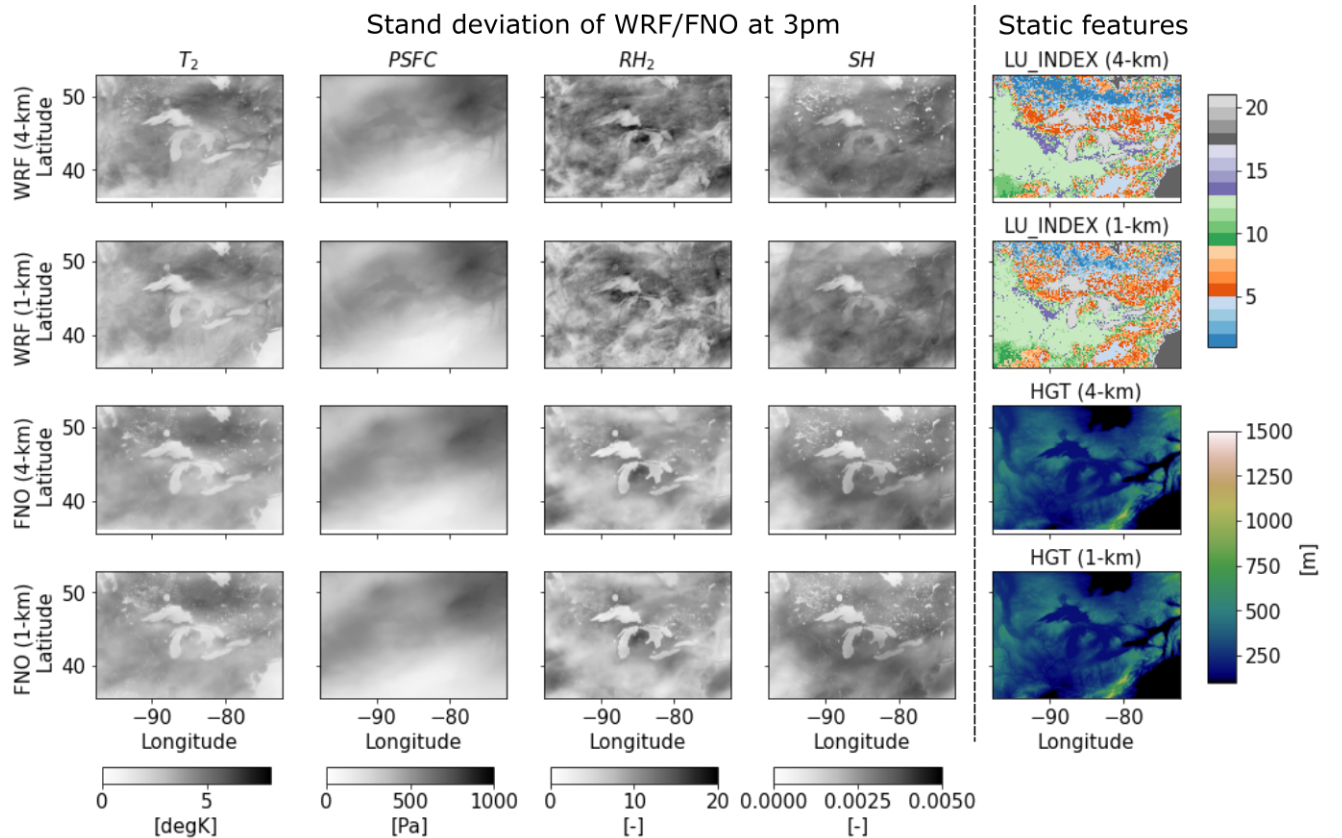


Figure S11. The standard deviation of WRF and FNO-cc (with $\alpha = 1$) surface heat simulation at 3pm of the entire modeling domain during August-23-2018 through August-31-2018 (i.e., the test period). The right column is the land use index (LU_INDEX) and terrain height (HGT) at both 1-km and 4-km scales. The left four columns are the simulations on the four surface heat variables at R1, including both WRF and FNO simulations at the two scales.

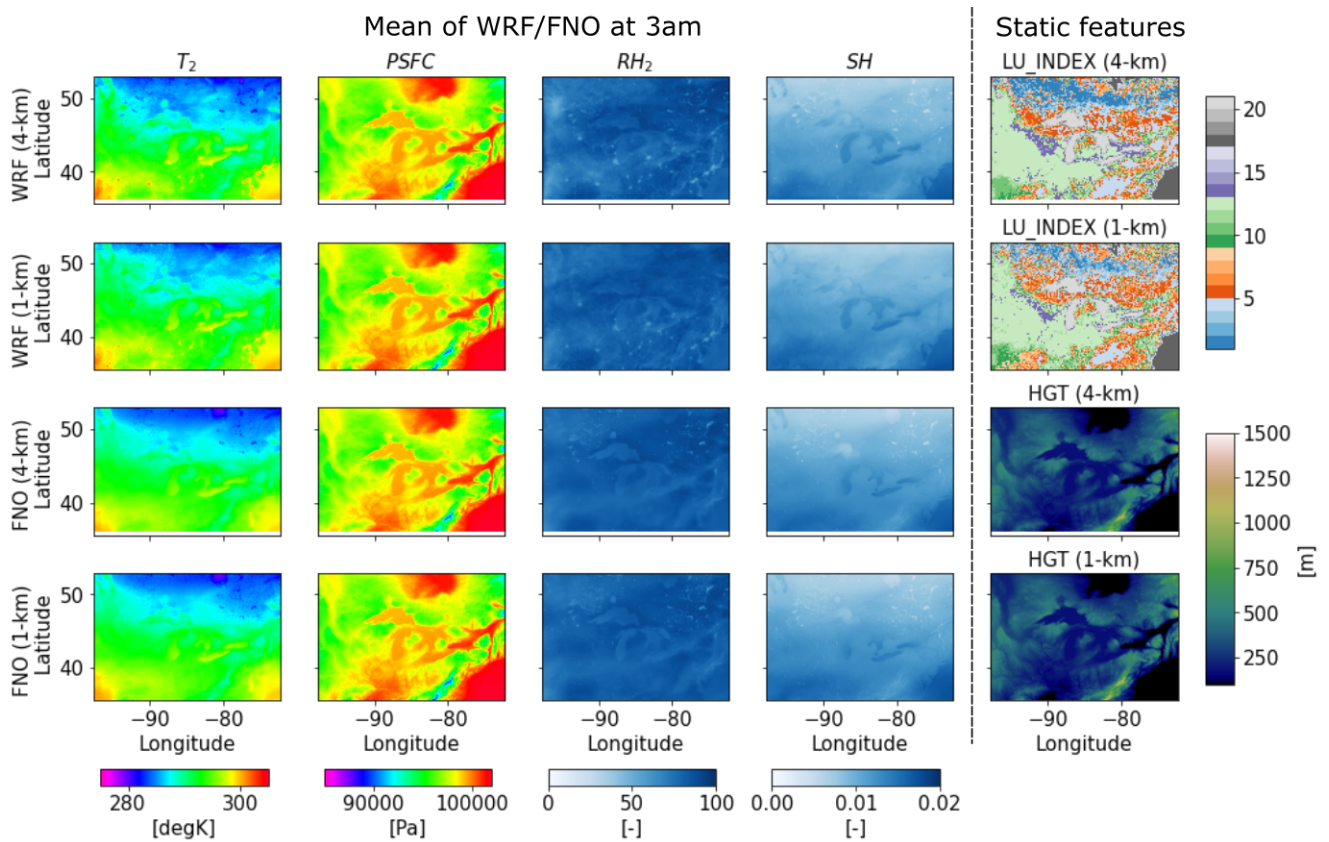


Figure S12. Temporally-averaged WRF and FNO-cc (with $\alpha = 1$) surface heat simulation at 3am of the entire modeling domain during August-23-2018 through August-31-2018 (i.e., the test period). The right column is the land use index (LU_INDEX) and terrain height (HGT) at both 1-km and 4-km scales. The left four columns are the simulations on the four surface heat variables at R1, including both WRF and FNO simulations at the two scales.

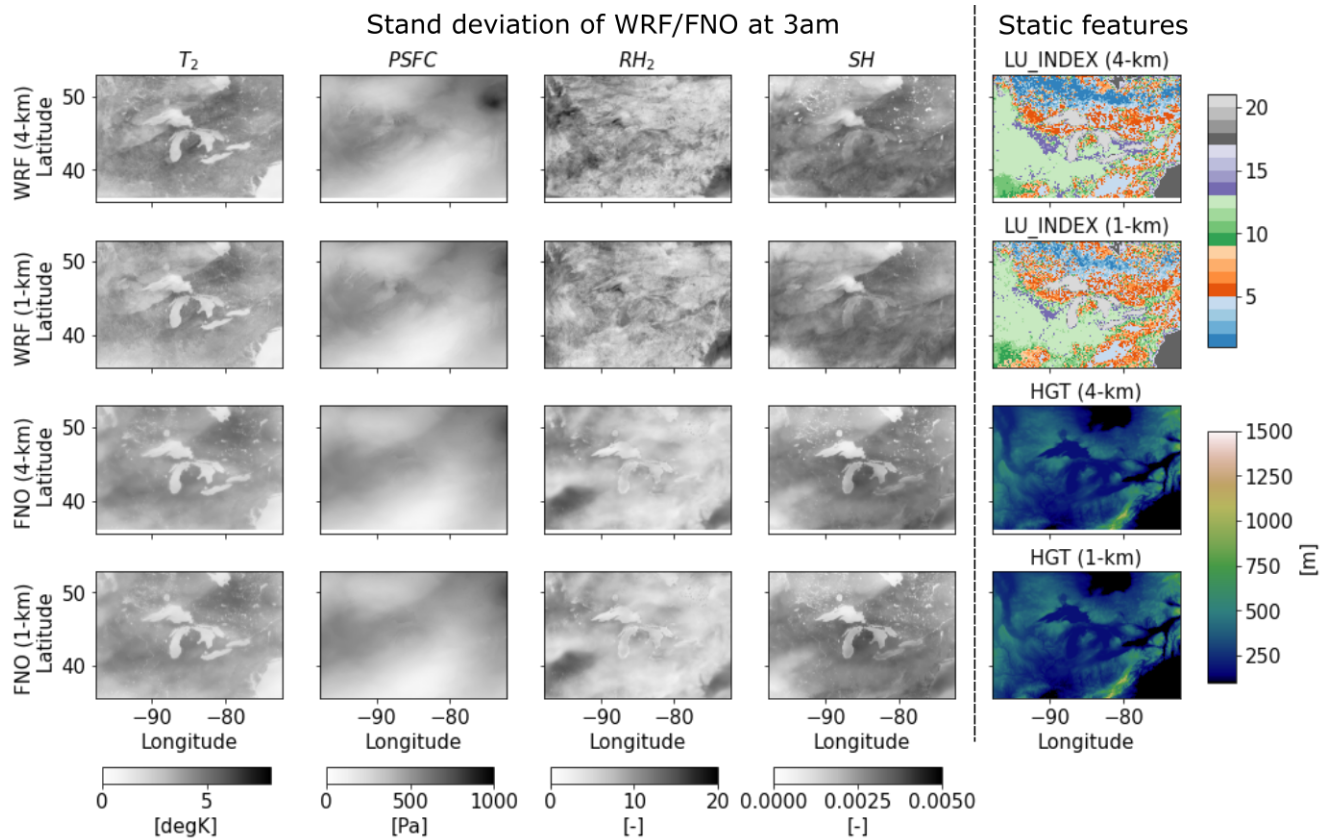


Figure S13. The standard deviation of WRF and FNO-cc (with $\alpha = 1$) surface heat simulation at 3am of the entire modeling domain during August-23-2018 through August-31-2018 (i.e., the test period). The right column is the land use index (LU_INDEX) and terrain height (HGT) at both 1-km and 4-km scales. The left four columns are the simulations on the four surface heat variables at R1, including both WRF and FNO simulations at the two scales.

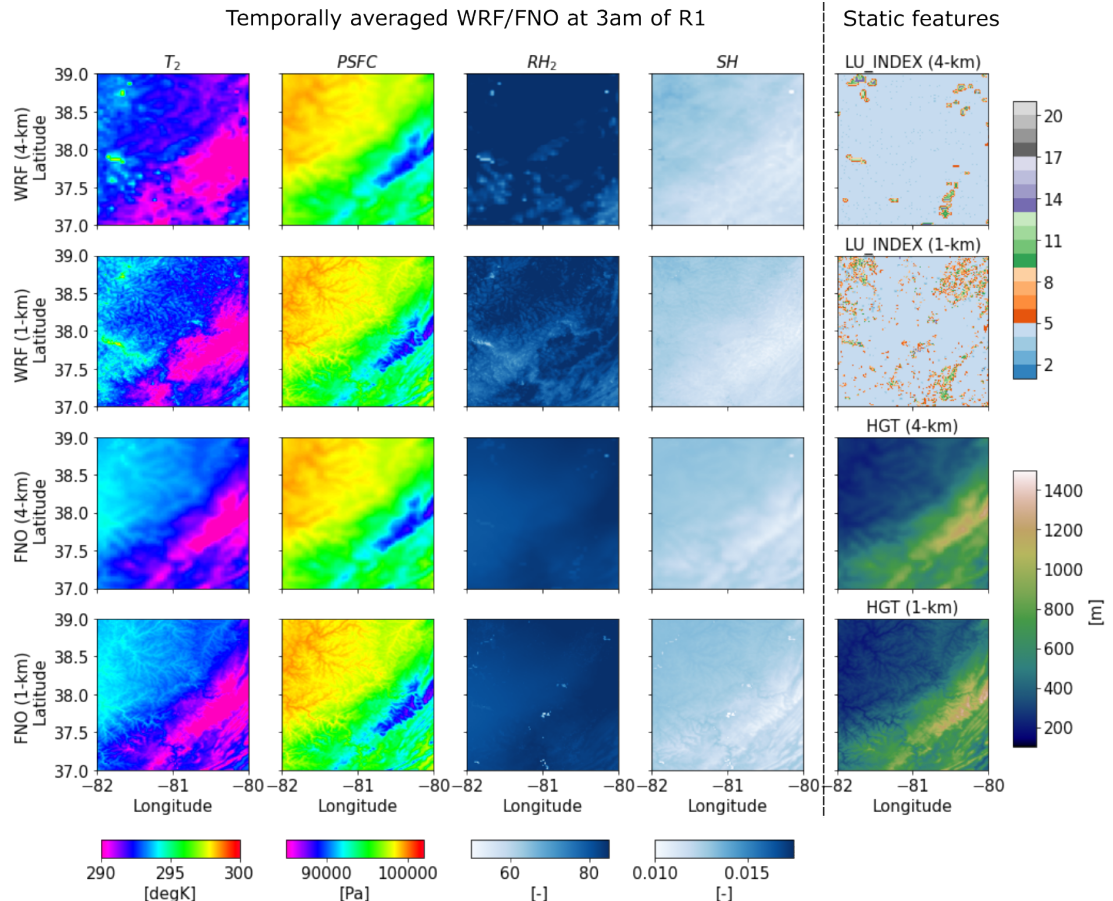


Figure S14. Temporally-averaged WRF and FNO-cc (with $\alpha = 1$) surface heat simulation at 3am of the subregion R1 during August-23-2018 through August-31-2018 (i.e., the test period). The right column is the land use index (LU_INDEX) and terrain height (HGT) at both 1-km and 4-km scales of R1. The left four columns are the simulations on the four surface heat variables at R1, including both WRF and FNO simulations at the two scales.

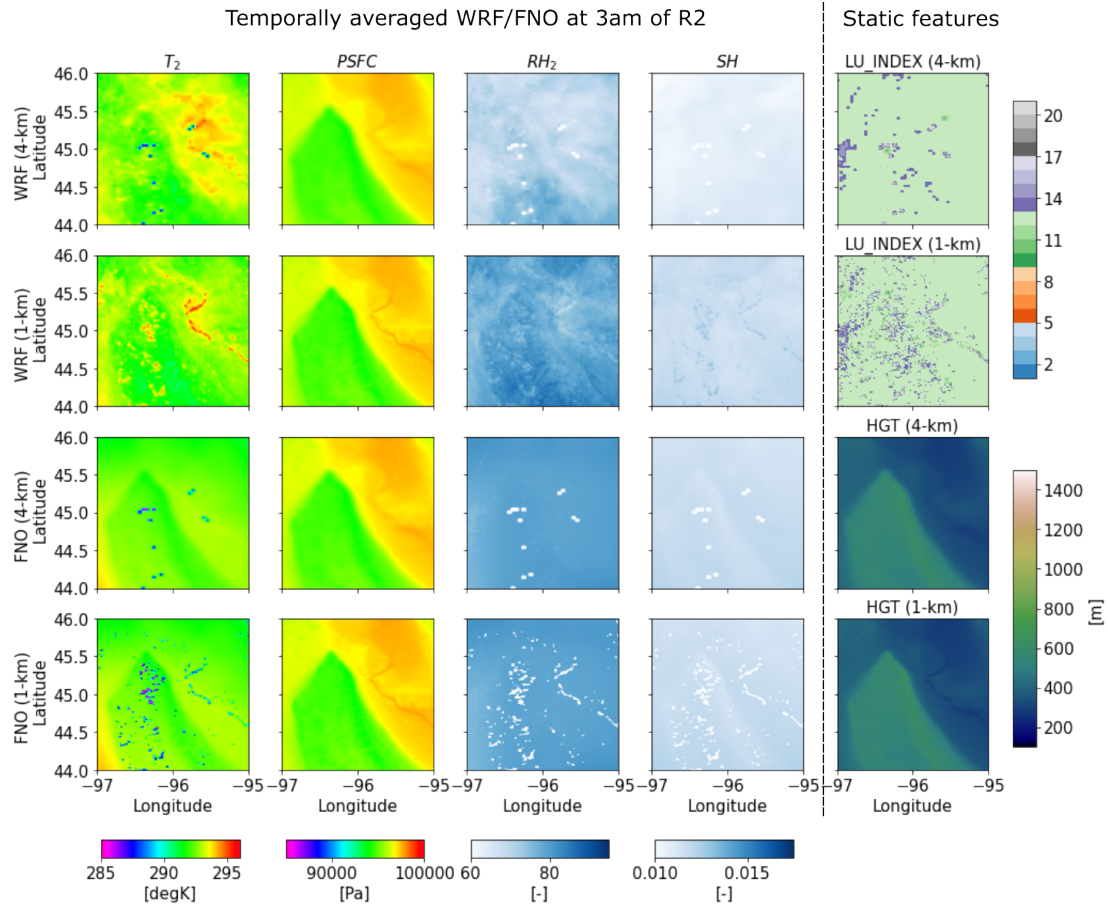


Figure S15. Temporally-averaged WRF and FNO-cc (with $\alpha = 1$) surface heat simulation at 3am of the subregion R2 during August-23-2018 through August-31-2018 (i.e., the test period). The right column is the land use index (LU_INDEX) and terrain height (HGT) at both 1-km and 4-km scales of R2. The left four columns are the simulations on the four surface heat variables at R1, including both WRF and FNO simulations at the two scales.

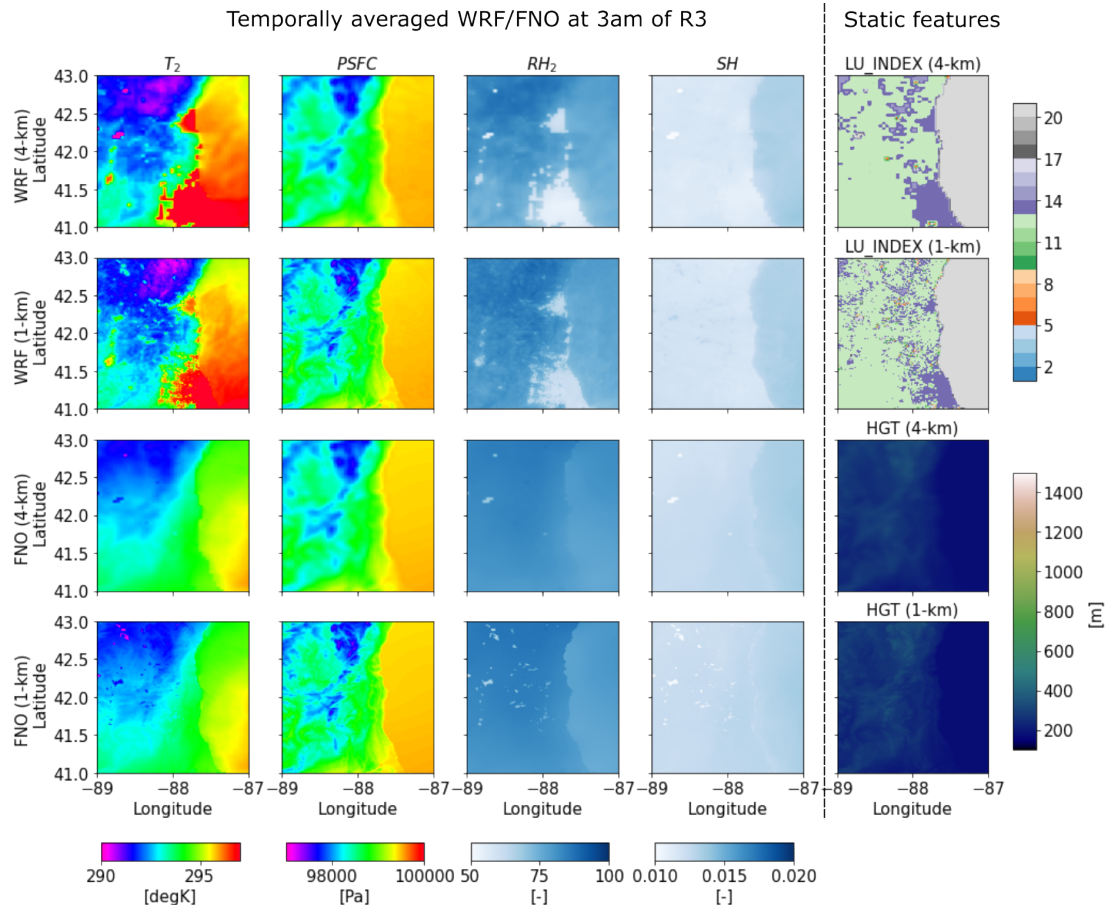


Figure S16. Temporally-averaged WRF and FNO-cc (with $\alpha = 1$) surface heat simulation at 3am of the subregion R3 during August-23-2018 through August-31-2018 (i.e., the test period). The right column is the land use index (LU_INDEX) and terrain height (HGT) at both 1-km and 4-km scales of R3. The left four columns are the simulations on the four surface heat variables at R1, including both WRF and FNO simulations at the two scales.

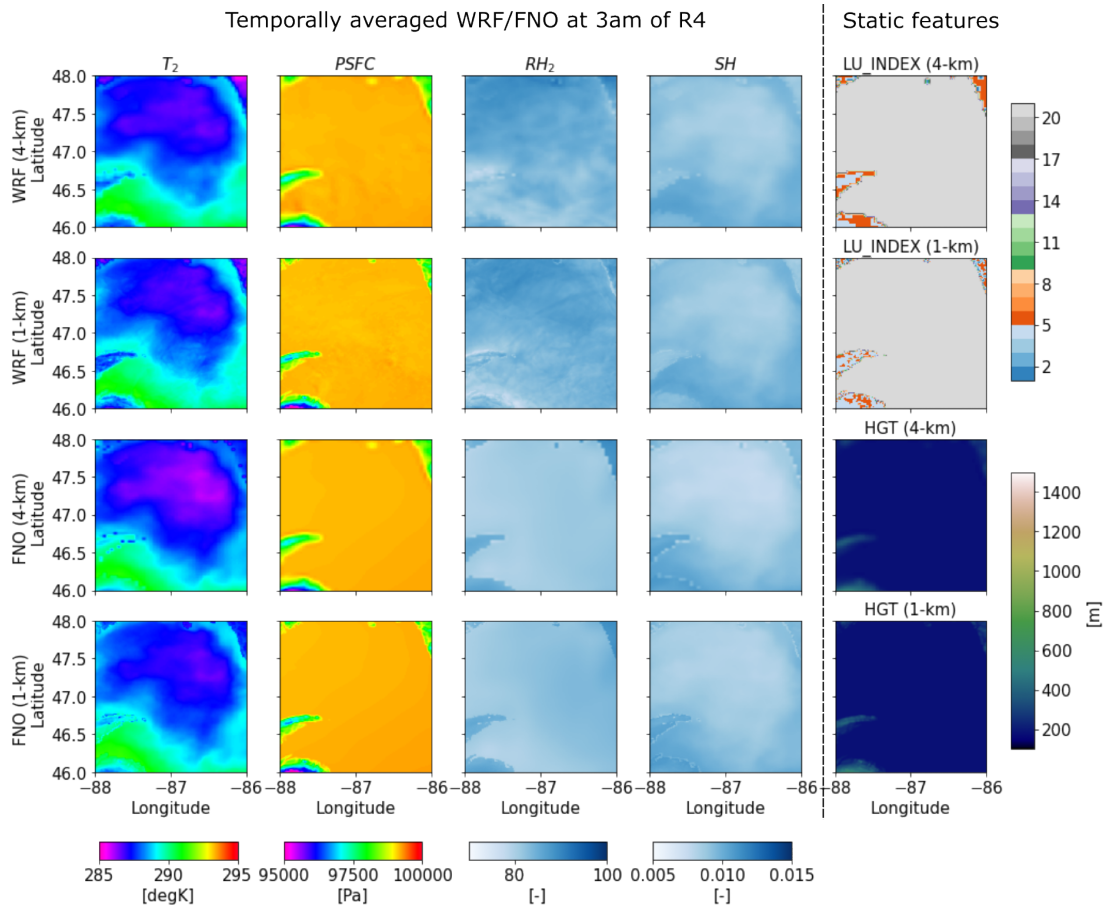


Figure S17. Temporally-averaged WRF and FNO-cc (with $\alpha = 1$) surface heat simulation at 3am of the subregion R4 during August-23-2018 through August-31-2018 (i.e., the test period). The right column is the land use index (LU_INDEX) and terrain height (HGT) at both 1-km and 4-km scales of R4. The left four columns are the simulations on the four surface heat variables at R1, including both WRF and FNO simulations at the two scales.